MATERIALS CHEMISTRY FRONTIERS

CHINESE CHEMICAL SOCIETY

ROYAL SOCIETY OF CHEMISTRY

RESEARCH ARTICLE

View Article Online
View Journal | View Issue

Cite this: *Mater. Chem. Front.*, 2024, **8**, 2539

Enhancing persistent radioluminescence in perovskite scintillators through trap defect modulation†

Xiaokun Li,‡[a] Huixi Guo,‡[bc] Yahuang Li,[a] Caihou Lin*[d] and Lili Xie*[a]

Flexible X-ray sensors utilizing persistent radioluminescence scintillators have garnered considerable interest in medical imaging and industrial non-destructive testing. However, persistent radioluminescence in scintillators is typically generated by releasing stored electrons from deep trap defects at high temperatures, significantly limiting X-ray imaging sensitivity. The requirement of high temperatures for thermally-stimulated radioluminescence to erase harmful X-ray memory also impedes the repeated use of flexible sensors. Here we report high-efficiency persistent radioluminescence at room temperature by modulating the depth and density distribution of trap defects through codoping with Mn^{2+} and Sb^{3+} in $CsCdCl_3$ scintillators. This results in a 20-fold increase in radioluminescence afterglow at room temperature, leading to significantly enhanced X-ray imaging sensitivity and facile erasure of harmful X-ray memory at relatively low temperatures for repeated use of the flexible sensors. Furthermore, the as-synthesized scintillators exhibit excellent resistance to thermal quenching, maintaining 96.63% radioluminescence efficiency at 493 K, and commendable stability concerning humidity and solvent exposure. Additionally, we fabricated flexible X-ray imaging sensors achieving high-resolution (20.0 lp mm^{-1}) imaging of irregulate objects at room temperature using $CsCdCl_3$:5%Mn^{2+}/0.1%Sb^{3+} crystals. These findings provide valuable insights into ion doping for the regulation of trap defects in scintillators, motivating the development of high-resolution time-lapse X-ray imaging sensors.

Received 13th January 2024,
Accepted 8th May 2024

DOI: 10.1039/d4qm00039k

rsc.li/frontiers-materials

1. Introduction

Flat-panel X-ray sensors have found widespread applications in safety inspection, industrial non-destructive testing, and medical diagnosis.[1–7] Recently, flat-panel-free flexible X-ray detectors have emerged for high-resolution imaging of irregular objects, utilizing persistent luminescence X-ray memory scintillators.[8–11] It is crucial to emphasize that conventional inorganic persistent luminescent phosphors, such as $SrAl_2O_4$:Dy/Eu^{2+}, $ZnGa_2O_4$:Cr^{3+} and ZnS:Cu^{2+}, necessitate rigorous preparation conditions and are typically activated by ultraviolet and visible excitations.[12–17] Consequently, they are unsuitable for applications in X-ray memory imaging.[18,19] In contrast, lanthanide-doped fluoride scintillators can store X-ray energy in their trap defects within crystal lattices and subsequently release it in the form of radioluminescence afterglow upon thermal, light, or force stimulation.[20–23] However, a substantial portion of X-ray-generated electrons is retained in deep traps and is only read out under relatively high temperatures.

Element dopants with varying ionic radius and valence states in inorganic materials can introduce lattice defects conducive to achieving persistent luminescence.[24–28] Nevertheless, there remains a limited understanding of the depth and density distribution of dopant-associated trap defects that influence the efficiency of persistent luminescence under thermal stimulation. Metal-halide perovskites, characterized by a low lattice energy (<1000 KJ mol^{-1}), a tolerant lattice and high yield hold promise as a substrate for achieving a tunable bandgap and low-temperature regulation of traps.[29–34] In the context of time-lapse X-ray imaging based on persistent luminescence scintillators, a lower temperature for thermally-stimulated persistent luminescence translates to faster and safer readout of X-ray imaging data. Therefore, achieving high-efficiency persistent luminescence at room temperature

[a] *Department of Health Inspection and Quarantine, the School of Public Health, Fujian Medical University, Fuzhou, 350122, Fujian, China. E-mail: 1006xielili@fjmu.edu.cn*
[b] *Department of Gastroenterology, Shengli Clinical Medical College of Fujian Medical University, Fuzhou, Fujian, China*
[c] *Department of Gastroenterology, Fujian Provincial Hospital, Fuzhou, Fujian, China*
[d] *Department of Neurosurgery, Union Hospital Affiliated of Fujian Medical University, Fuzhou 350001, Fujian, China. E-mail: grouplin@fjmu.edu.cn*

† Electronic supplementary information (ESI) available. See DOI: https://doi.org/10.1039/d4qm00039k

‡ These authors have contributed equally to this work.

without additional heating is of particular interest. Furthermore, enhancing the persistent luminescence intensity and duration through the doping of ions in metal-halide perovskites to adjust defect traps will lead to high-sensitivity X-ray imaging.[35–37]

Here we present an effective strategy to modulate the depth and density distribution of trap defects in $CsCdCl_3$ scintillators through codoping with Mn^{2+} and Sb^{3+}, significantly enhancing their persistent radioluminescence at room temperature. This unique feature not only leads to improved sensitivity of X-ray imaging at room temperature but also allows for the facile erasure of harmful X-ray memory at relatively low temperatures, enabling repeated use of the flexible sensors. The as-synthesized $CsCdCl_3$:Mn^{2+}/Sb^{3+} exhibits excellent resistance to thermal quenching and commendable stability concerning temperature, humidity, and solvent exposure. Flexible X-ray sensors were further fabricated to achieve time-lapse X-ray imaging with high resolution of 20.0 lp mm^{-1}.

2. Experimental section

2.1. Materials

Cesium chloride (CsCl, 99.99%), cadmium chloride ($CdCl_2$, 99.99%), manganese(II) chloride ($MnCl_2$, 99.99%), antimony trichloride ($SbCl_3$, 99.98%), zinc chloride ($ZnCl_2$, 99.95%), bismuth chloride ($BiCl_3$, 99.99%), zirconium chloride ($ZrCl_4$, 99.9%), and tellurium tetrachloride ($TeCl_4$, 99.9%) were purchased from Aladdin Biochemical Technology. Hydrochloric acid (AR), cyclohexane (AR), methylbenzene (AR), *N*,*N*-dimethylformamide (AR), and ethanol (AR) were purchased from Sinopharm Co. Ltd. Sylgard 184 PDMS elastomer kit was purchased from Dow Corning. Unless otherwise stated, all chemicals were used without further treatment.

2.2. Characterization

The morphology and element distribution of the synthesized samples were analyzed using a scanning electron microscope with tungsten filament (SEM, Quanta 250). Conventional scanning tests on perovskite powders were conducted with an X-ray powder diffractometer (XRD, DY1602), with the scanning angle range set to 5–80°. X-ray photoelectron spectroscopy (XPS, ESCALAB 250) was used to characterize the elemental composition and valence state of perovskite crystals. Electron paramagnetic resonance (EPR, EPR200M) spectra are measured by an EPR instrument at a magnetic field modulation frequency of 100 kHz. For optical analysis, diffuse reflectance spectral analysis in the range of 200–600 nm was performed using a UV-Visible-NIR scanning spectrophotometer (UV-Visible-NIR, Cary 7000). Thermogravimetric analysis (TGA) and differential scanning calorimetry (DSC) were carried out using a simultaneous thermal analyzer (STA, STA449C/6/G) at a heating rate of 10 °C min^{-1}. Radioluminescence spectra and afterglow luminescence decay curves were measured by a fluorescence spectrophotometer (FS5) equipped with an X-ray tube, excited at 50 kV and 80 μA. Excitation spectra and emission spectra under ultraviolet (UV) excitation of the perovskite crystal were tested using a fluorescence spectrometer (FLS 980). The sample thermoluminescence glow curve was obtained by the FS5 fluorescence spectrometer and a hot/cold stage temperature control device (HFS 600) at 60 K min^{-1}. Photographs of the crystals were recorded using a camera (Nikon D850). The microcomputer control electron universal testing machine (TSE104C) was used for tensile testing of a flexible scintillator screen.

2.3. Synthesis of $CsCdCl_3$:xMn^{2+} (x = 0–30%) crystals

$CsCdCl_3$:Mn^{2+} perovskite crystals were synthesized using a hydrothermal method. The procedure involved placing a mixture of 3 mmol CsCl, 3 mmol $CdCl_2$, and x% mmol $MnCl_2$ into a 25 mL polytetrafluoroethylene liner. Subsequently, 12 mL of concentrated hydrochloric acid was added for dissolution. The liner was sealed within a stainless steel autoclave, heated to 180 °C in an electric blast drying oven, maintained at this temperature for 10 hours, and then slowly cooled to room-temperature over 12 hours. Finally, the crystals underwent a purification process, being washed 2–3 times with absolute ethanol, and were dried at 60 °C overnight.

2.4. Synthesis of $CsCdCl_3$:5%Mn^2/0.1%R^{n+} (R = Zn^{2+}, Bi^{3+}, Sb^{3+}, Zr^{4+}, Te^{4+}) crystals

The synthetic procedure for $CsCdCl_3$:5%Mn^{2+}/0.1%R^{n+} (R = Zn^{2+}, Bi^{3+}, Sb^{3+}, Zr^{4+}, Te^{4+}) crystals was identical to the synthesis of $CsCdCl_3$: xMn^{2+} (x = 0–30%) crystals.

2.5. Synthesis of $CsCdCl_3$:5%Mn^{2+}/ySb^{3+} (x = 0–1%) crystals

The synthetic procedure for $CsCdCl_3$:5%Mn^{2+}/ySb^{3+} (y = 0–1%) crystals was identical to the synthesis of $CsCdCl_3$:xMn^{2+} (x = 0–30%) crystals.

2.6. Preparation of $CsCdCl_3$:5%Mn^{2+}/0.1%Sb^{3+}@PDMS flexible scintillation screen

The PDMS elastomer matrix was mixed with the curing agent at a mass ratio of 10 : 1, and a certain amount of ground $CsCdCl_3$:5%Mn^{2+}/0.1%Sb^{3+} powder was added to mix thoroughly. Finally, the mixture was deposited by blade coating and cured at 80 °C for 4 hours to obtain a flexible scintillation screen.

2.7. Thermoluminescence glow curves measurement

Firstly, the samples were heated until no afterglow signal was generated. The samples were subsequently cooled to the excitation temperature (230–430 K) and irradiated with X-ray excitation for 3 min. The sample temperature was lowered to 165 K before each test and then heated to 580 K at a heating rate of 60 K min^{-1} to obtain thermoluminescence glow curves.

2.8. Tensile testing

In the tensile tests, the stretching speed was set to 10 mm min^{-1} until it broke. The slope of the initial linear region of the stress–strain curve can be estimated to obtain Young's modulus. Here, the ratio of the length change to the initial length can be used to

obtain the strain, while the force divided by the cross-sectional area of the sample can be used to obtain the stress.

2.9. Calculate the value of light yield

First, the thickness absorption functions of CsI:Tl and $CsCdCl_3$:Mn^{2+}/Sb^{3+} scintillator at 22 keV were calculated. Then, the $CsCdCl_3$:Mn^{2+}/Sb^{3+} scintillator power was pressed to the same shape as the standard CsI:Tl crystal with a diameter of 7 mm and thickness of 3 mm. To quantify the light yield, standard CsI:Tl scintillators are used as a reference with 60 000 photons per MeV, the light yield of $CsCdCl_3$:Mn^{2+}/Sb^{3+} can be calculated by the following formula:

$$LY_{CsCdCl_3:Mn^{2+}/Sb^{3+}} = \frac{I_2}{b}/\frac{a}{I_1} \cdot LY_{CsI:Tl}$$

where I_1 and I_2 are the radioluminescence intensities of the CsI:Tl crystals and the $CsCdCl_3$:Mn^{2+}/Sb^{3+} crystals, a and b are the X-ray attenuation efficiencies of the CsI:Tl crystal and the $CsCdCl_3$:Mn^{2+}/Sb^{3+} crystals.

2.10. Computational details

All calculations were performed using the VASP software package with the projector augmented wave method. The Perdew–Berke–Ernzerhof (PBE) generalized gradient approximation was employed to describe the electronic interactions, with a wave function cutoff energy set at 520 eV. Full relaxation of all atoms was conducted, ensuring that the maximum force on each relaxed atom was below 0.02 eV $Å^{-1}$ and the energy converged to less than 10^{-5} eV. For density functional theory (DFT) calculations, a Γ-centered k-point grid with dimensions of 3 × 3 × 2 was utilized. To construct the crystal with Mn^{2+} doping, the lattice parameters in each direction were set to a minimum of 10 Å.

3. Results and discussion

3.1. Enhancing radioluminescence afterglow at room temperature

In a hexagonal $CsCdCl_3$ crystal, Cd atoms exhibit dual coordination crystal environments—either forming $[Cd_2Cl_9]^{5-}$ by sharing a triangular surface within a bipyramidal structure or adopting a typical $[CdCl_6]^{4-}$ arrangement by coordinating with six chlorine atoms (Fig. 1a).[38] Our simulation results suggest that lattice distortion may arise due to differences in the valence state and ionic radius of Sb^{3+} (coordination number, CN = 6, ionic radius r = 0.76 Å) and Mn^{2+} (CN = 6, r = 0.83 Å) with Cd^{2+} (CN = 6, r = 0.95 Å) resulting from the random doping of Mn^{2+} and Sb^{3+} into Cd^{2+} sites.[39] To validate our hypothesis, we prepared Mn^{2+} and Sb^{3+}-codoped $CsCdCl_3$ particles using a hydrothermal method (Fig. S1a, ESI†). XRD analysis reveals gradual shifts in diffraction peaks to higher angles with increasing concentrations of Sb^{3+} and Mn^{2+} ions (Fig. 1b and Fig. S1b, ESI†), indicating the replacement of Cd^{2+} ions with Mn^{2+} and Sb^{3+} ions. Energy dispersive spectrometer (EDS) results demonstrate the uniform doping of Mn^{2+} and Sb^{3+} ions into the $CsCdCl_3$ matrix (Fig. S2, ESI†). Characteristic peaks in the binding energy of Mn^{2+} $2p_{1/2}$ and $2P_{2/3}$, and Sb^{3+} $3d_{3/2}$ and $3d_{5/2}$ of $CsCdCl_3$:Mn^{2+}/Sb^{3+} from X-ray photoelectron spectroscopy (XPS) confirm the consistent valence state of the doped elements (Fig. S3, ESI†).[39,40] Importantly, X-ray-induced defect traps in the as-synthesized crystals can be adjusted from deep to shallow by introducing different valence ions, as evidenced by thermal simulation from the high-temperature region to the room-temperature region (Fig. 1c). Remarkably, the presence of Sb^{3+} ions significantly enhances the afterglow intensity of the crystal at room temperature, showing an increase of 20 times (Fig. 1d). The duration and intensity of radioluminescence afterglow from the Sb^{3+} doped samples are significantly superior to those from the undoped samples at room temperature (Fig. 1e).

3.2. Optical properties of efficient radioluminescence afterglow

We further investigated the optical characteristics of radioluminescence afterglow in $CsCdCl_3$:Mn^{2+}/Sb^{3+} upon X-ray irradiation. Under X-ray irradiation, the afterglow intensity reached the strongest when the concentration of 5%Mn^{2+} doped into the $CsCdCl_3$ crystal lattice (Fig. S4a, ESI†). Our experimental results demonstrated that, upon doping with Zn^{2+}, Bi^{3+}, Sb^{3+}, Zr^{4+}, and Te^{4+} ions, the strongest radioluminescence afterglow was observed in Sb^{3+}-doped $CsCdCl_3$:5 mol%Mn^{2+}, with no discernible impact on the excited state of Mn^{2+} ion (Fig. 2a and Fig. S4b–d, S5, ESI†). The radioluminescence of $CsCdCl_3$ crystal upon X-ray irradiation exhibited a broadband emission peak at 2.13 eV with a half-maximum FWHM of 0.28 eV, originating from the self-trapped exciton (STE) excited state (Fig. S6a–c, ESI†).[41–44] Compared with the $CsCdCl_3$: Mn^{2+}, the $CsCdCl_3$:Mn^{2+}/Sb^{3+} exhibit similar luminescence properties, and the optimal dopant amount of 0.1 mol% Sb^{3+} led to a remarkable 20-fold enhancement in the afterglow intensity (Fig. 2b and Fig. S6d–i, ESI†). After X-ray excitation, the afterglow emission of $CsCdCl_3$:Mn^{2+}/Sb^{3+} crystals persisted for 120 minutes at room temperature (Fig. 2c). In contrast, afterglow luminescence in $CsCdCl_3$:Mn^{2+} crystals rapidly decreased after the cessation of X-ray excitation (Fig. S7a and b, ESI†). The electron paramagnetic resonance (EPR) spectra of $CsCdCl_3$: Mn^{2+} showed no obvious changes upon the introduction of Sb^{3+} (Fig. S7c, ESI†). The quantum yield of the as-synthesized $CsCdCl_3$:Mn^{2+}/Sb^{3+} crystal was measured as high as 87.21% (Fig. S7d, ESI†).[45,46] It is worth noting that the actual ion content in the lattice detected by inductively coupled plasma (ICP) is slightly lower than the theoretical content (Table S1 and S2, ESI†).

The X-ray absorption coefficient of $CsCdCl_3$:Mn^{2+}/Sb^{3+} is comparable to that of conventional commercial scintillators such as CaF_2:Eu, $YAlO_3$:Ce, $Lu_2Y_2SiO_5$:Ce, and $Bi_4Ge_3O_{12}$, while its radioluminescence outperforms them (Fig. 2d-e and Fig. S8a, ESI†). A standard scintillator of CsI:Tl (60 000 photons per MeV) as reference, the light yield of $CsCdCl_3$:Mn^{2+}/Sb^{3+} is measured at 74 828 photons per MeV, which surpasses the majority of commercial avaliable scintillator (Fig. S8b and c, ESI†).[47] We assessed the detection capability of these

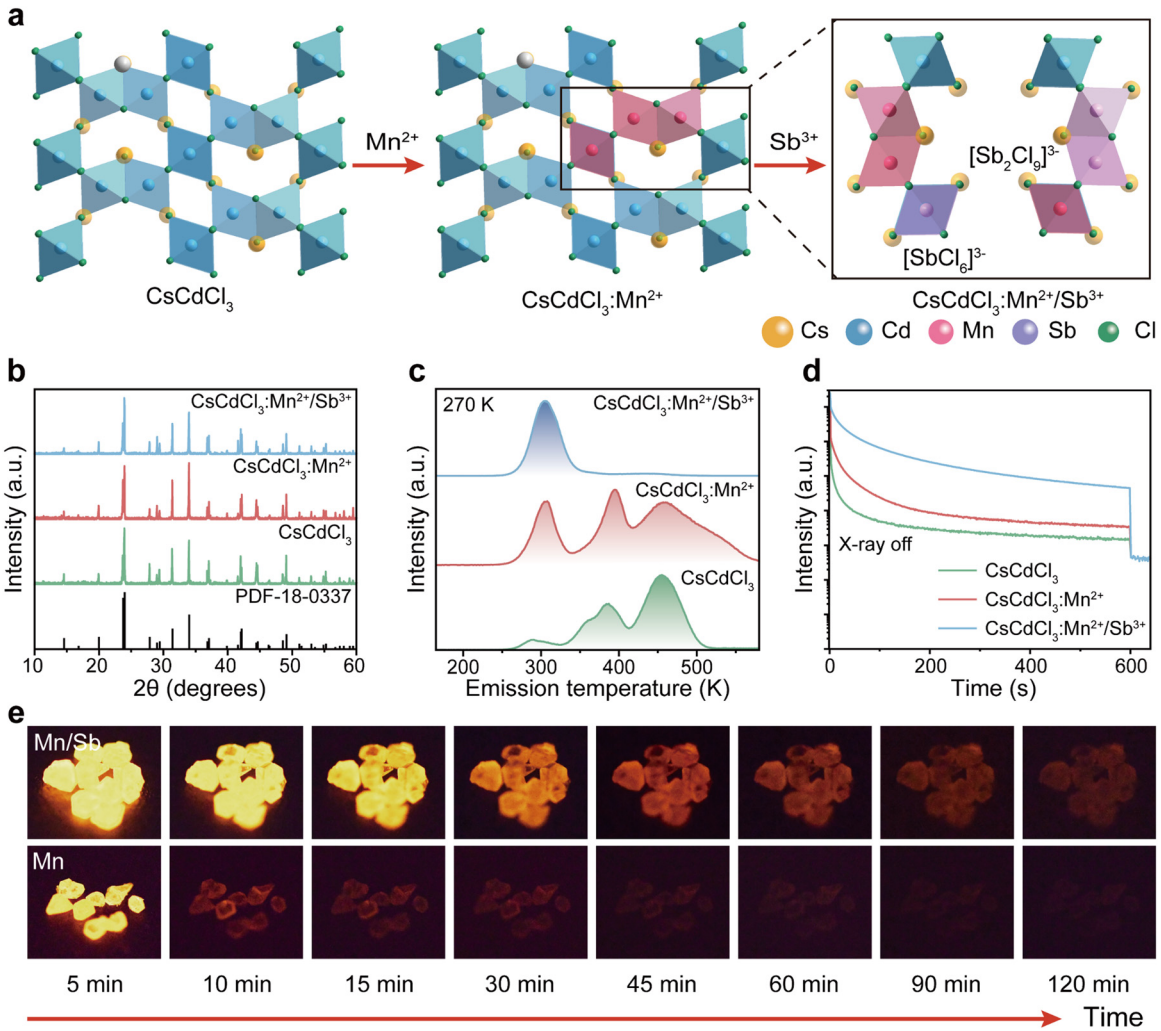

Fig. 1 Trap defect engineering and persistent luminescence in $CsCdCl_3$:5%Mn^{2+}/0.1%Sb^{3+} crystals. (a) Crystal structure of hexagonal $CsCdCl_3$ and its evolution through Mn^{2+} and Sb^{3+} doping. (b) XRD patterns of $CsCdCl_3$, $CsCdCl_3$:5%Mn^{2+} and $CsCdCl_3$:5%Mn^{2+}/0.1%Sb^{3+}. (c) Trap distribution of $CsCdCl_3$, $CsCdCl_3$:5%Mn^{2+} and $CsCdCl_3$:5%Mn^{2+}/0.1%Sb^{3+}. Thermoluminescence glow curves measured at a heating rate of 60 K min^{-1} after X-ray irradiation. (d) Comparison of radioluminescence afterglow decay of $CsCdCl_3$, $CsCdCl_3$:5%Mn^{2+} and $CsCdCl_3$:5%Mn^{2+}/0.1%Sb^{3+} crystals at room temperature after X-ray excitation for 3 min (50 kV). (e) Afterglow photographs of $CsCdCl_3$:5%Mn^{2+} and $CsCdCl_3$:5%Mn^{2+}/0.1%Sb^{3+} at different times after the removal of X-ray at room temperature.

scintillators in response to X-ray irradiation, and the calculated detection limit was 29.9 nGy s^{-1}, approximately 184 times lower than the dosage used for medical diagnostics (5.5 μGy s^{-1}) (Fig. 2f and Fig. S8d, ESI†).[48] To exclude the influence of chance factor on the experimental results, all the stability experiments were repeated three times and error analysis was performed. The radiation on–off cycles of 2400 s were tested under a 278 μGy s^{-1} dose of X-ray excitation and exhibited a negligible radioluminescence intensity decline. The increased intensity of the front part of on–off curve is caused from the process of releasing photons after charging the defect (Fig. 2g and Fig. S8e, ESI†). Moreover, even after soaking in an extreme water environment for 5 days, the radioluminescence intensity remained at 85% (Fig. 2h). As the Fig. 2i and Fig. S8f (ESI†) shown, the $CsCdCl_3$:Mn^{2+}/Sb^{3+} crystal demonstrated excellent solvent stability when immersed in various polar and non-polar solvents for 12 h. The TG curve indicates that the structure of $CsCdCl_3$:Mn^{2+}/Sb^{3+} crystal remains very stable before 575 °C (Fig. S8g, ESI†). These results demonstrate that $CsCdCl_3$:Mn^{2+}/Sb^{3+} is a promising scintillator for X-ray imaging and radiation detection. Additionally, the doping of Sb^{3+} significantly increases the optical absorption edge band of $CsCdCl_3$:5%Mn^{2+} (Fig. S8h, ESI†).

3.3. Mechanism investigation of energy trapping regulation

To understand the mechanisms governing energy traps, we delved into the study of thermal luminescence (TL), thermally stimulated luminescence (TSL) decay curves, and optically stimulated luminescence (OSL) decay curves. The full width at half maximum (FWHM) and intensity of TL curves can indicate trap distribution and depth. With the introduction of additional Sb ions into $CsCdCl_3$:Mn^{2+} crystals, the FWHM of

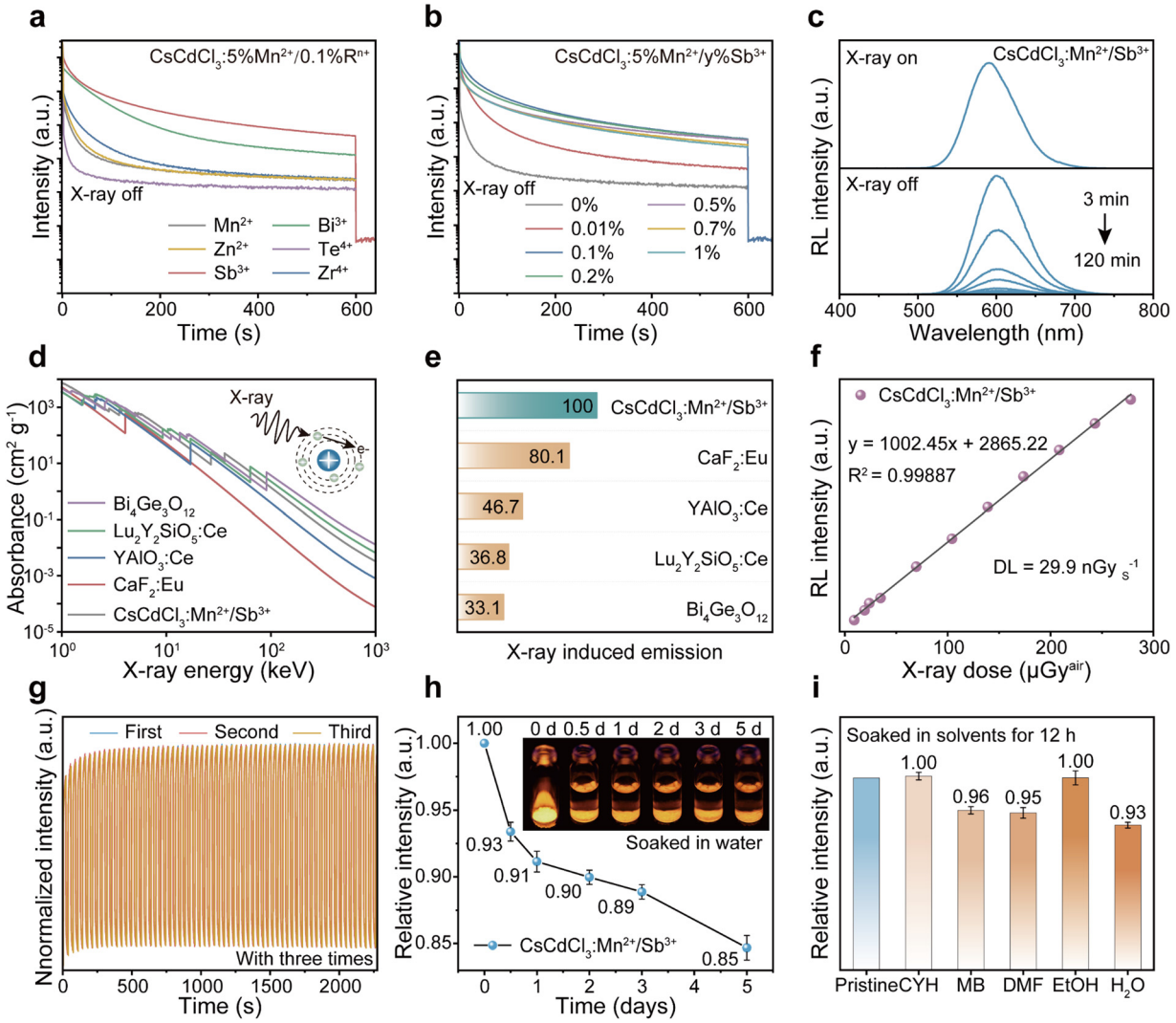

Fig. 2 DFT calculation and radioluminescence properties of the as-synthesized perovskite scintillators. (a) and (b) Afterglow decay curve of $CsCdCl_3$:5%Mn^{2+}/0.1%R^{n+} (R = Zn^{2+}, Bi^{3+}, Sb^{3+}, Zr^{4+}, Te^{4+}) and $CsCdCl_3$:5%Mn^{2+}/*y*%Sb^{3+}(*y* = 0–1%) at room temperature after cessation of X-ray excitation (50 kV, 3 min). (c) Radioluminescence (RL) spectra of $CsCdCl_3$:5%Mn^{2+}/0.1%Sb^{3+} crystals within 120 min at room temperature after cessation of X-ray excitation (50 kV, 3 min). (d) X-ray absorption coefficients of $Bi_4Ge_3O_{12}$, $Lu_2Y_2SiO_5$:Ce, $YAlO_3$:Ce, CaF_2:Eu and $CsCdCl_3$:5%Mn^{2+}/0.1%Sb^{3+} as a function of photon energy. The inset shows a schematic of X-ray-induced photoionization. (e) Comparison of radioluminescence intensity of $CsCdCl_3$:Mn^{2+}/Sb^{3+} and commercial scintillator materials. (f) Dose rate dependence of the radioluminescence intensity of $CsCdCl_3$:Mn^{2+}/Sb^{3+} in the range of 0.688 to 278 μGy s^{-1}. The detection limit (DL) is calculated using the 3σ/slope method. (g) Radioluminescence intensity of $CsCdCl_3$:Mn^{2+}/Sb^{3+} with repeated on–off cycles of X-ray excitation with three repetitions (Em = 592 nm, 50 kV). (h) Radioluminescence properties of $CsCdCl_3$:5%Mn^{2+}/0.1%Sb^{3+} were compared after soaking in water for 0, 0.5, 1, 3, 5 days. The inset shows a radioluminescence photograph of the crystals soaked in water for different days under X-ray irradiation. (i) The radioluminescence properties of $CsCdCl_3$:5%Mn^{2+}/0.1%Sb^{3+} were compared after soaking in different solvents for 12 h. CYH stands for Cyclohexane, MB stands for methylbenzene, DMF stands for *N*,*N*-dimethylformamide, and EtOH stands for ethanol, respectively.

the TL curve in the room temperature region broadens, and the peak in the high-temperature region transitions towards room temperature (Fig. 3a, b and Fig. S9a, ESI†). Remarkably, the majority of electrons stored in the defect can be released before reaching room temperature at 297 K, while a few electrons remain stored in the deep defect (Fig. S9b, ESI†). After X-ray irradiation, repeated stimulation of $CsCdCl_3$:5%Mn^{2+}/0.1%Sb^{3+} by 980-nm laser can release electrons stored in deep defects (Fig. S9c, ESI†). The trap depth of $CsCdCl_3$, $CsCdCl_3$:Mn^{2+} and $CsCdCl_3$:Mn^{2+}/Sb^{3+} were calculated using the Hoogenstraaten method:[49]

$$\frac{\beta E}{k_B \cdot T_m^2} = s \exp\left(\frac{-E}{k_B \cdot T_m}\right)$$

Where β (K s^{-1}) represents the heating rate, E (eV) denotes the trap depth, k_B stands for the Boltzmann constant, T_m (K) indicates the peak temperature in the TL glow curves, and s (s^{-1}) signifies the frequency factor. The trap depth can be obtained by linear fitting of $\ln(T_m^2/\beta)$ against $1/(k_B \cdot T_m)$ (Fig. S10, ESI†). The trap depths were 0.47 ± 0.05 eV, 0.71 ± 0.04 eV,

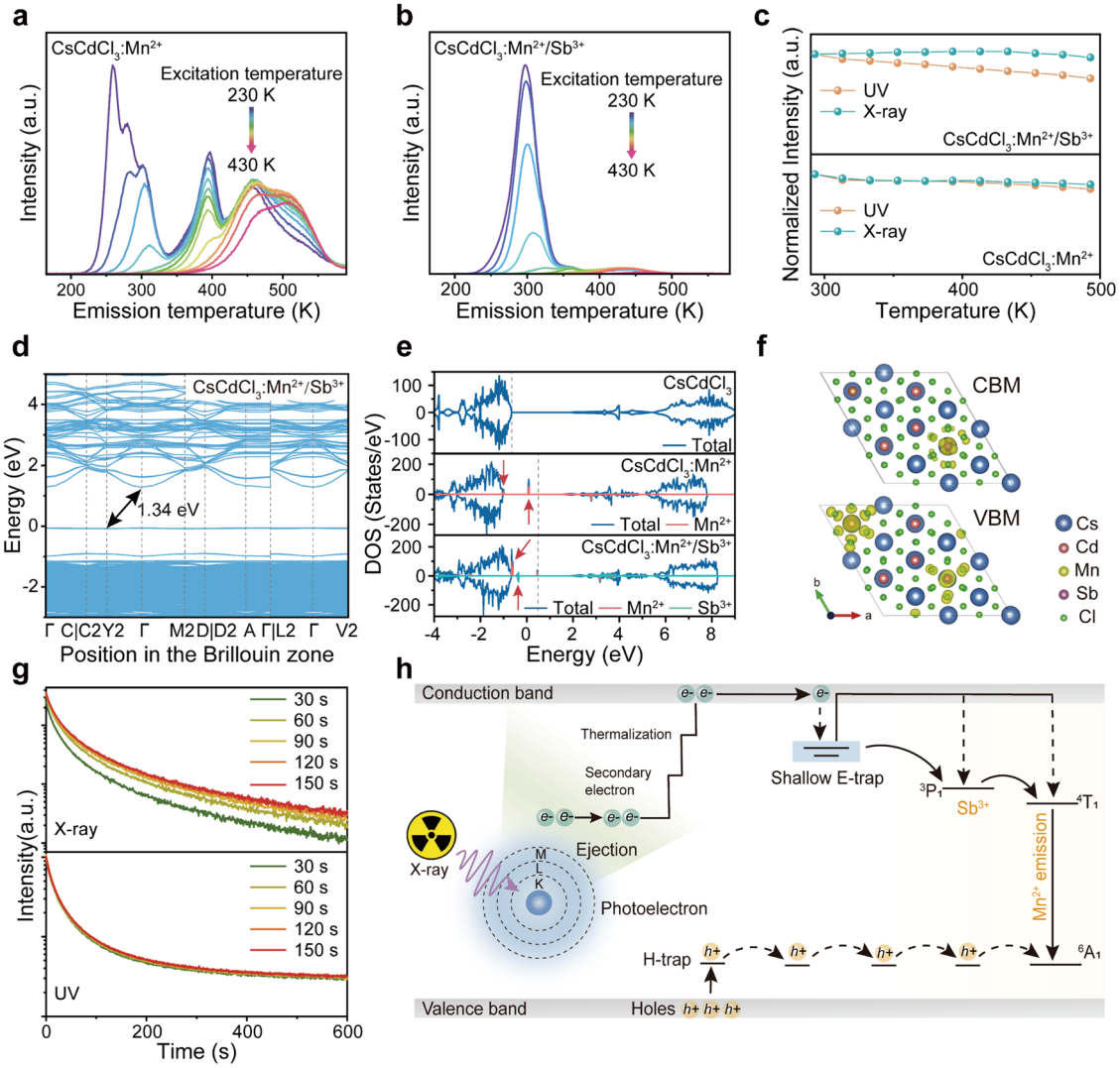

Fig. 3 Mechanism investigation of persistent radioluminescence in $CsCdCl_3$:5%Mn^{2+}/0.1%Sb^{3+} Crystal. (a) and (b) Thermoluminescence glow curves of $CsCdCl_3$:5%Mn^{2+} and $CsCdCl_3$:5%Mn^{2+}/0.1%Sb^{3+} in the temperature range of 230 to 430 K after cessation of X-ray excitation (50 kV, 3 min). The heating rate is 60 K min^{-1}. (c) Comparison of luminescence intensities of $CsCdCl_3$:5%Mn^{2+} and $CsCdCl_3$:5%Mn^{2+}/0.1%Sb^{3+} in the range 293 to 493 K under X-ray and UV excitation. (d) Calculated band structure of $CsCdCl_3$:5%Mn^{2+}/0.1%Sb^{3+}. (e) The density of states of pristine $CsCdCl_3$ (top), $CsCdCl_3$:5%Mn^{2+} (middle) and $CsCdCl_3$:5%Mn^{2+}/0.1%Sb^{3+} (bottom). Note that for comparison purposes, the value of the Sb-resolved state density is amplified tenfold. (f) The charge density of $CsCdCl_3$:5%Mn^{2+}/0.1%Sb^{3+} at valence band maximum (VBM) and conduction band minimum (CBM). (g) Comparison of afterglow attenuation curves of $CsCdCl_3$:5%Mn^{2+}/0.1%Sb^{3+} crystals at different excitation times after cessation of X-ray and UV excitation. (h) Proposed mechanism of persistent radioluminescence of $CsCdCl_3$:5%Mn^{2+}/0.1%Sb^{3+} at room temperature. Under X-ray excitation, atoms are excited to produce many high-energy electrons and holes. Some of the electrons are transferred directly to the luminescence center. While the other part is stored in traps, electrons in shallow traps are re-released to the luminescence center at room temperature, producing radioluminescence.

0.86 ± 0.06 eV and 1.09 ± 0.03 eV for $CsCdCl_3$, 0.50 ± 0.04 eV, 0.87 ± 0.04 eV and 1.01 ± 0.04 eV for $CsCdCl_3$:Mn^{2+}, 0.50 ± 0.04 eV, 0.87 ± 0.04 eV and 1.01 ± 0.04 eV for $CsCdCl_3$:Mn^{2+}/Sb^{3+}.

The density of the defect can be calculated by the following formula:[50,51]

$$n = \omega I_m / \{\beta \times 2.52 + 10.2 \times (\mu_g - 0.42)\}$$

where ω is the full width at half maximum (FWHM) of the TL band. I_m is the intensity of the TL peak, and β represents the heating rate. Attributed to the conducting of Gaussian fitting, the deconvoluted peaks are symmetrical, thus μ_g = 0.5. The heating rate (β) is 60 K min^{-1} (Fig. S11, ESI†). As the Table S3 (ESI†) shows, introducing additional Sb^{3+} ions increases the density of shallow defects, which leads to enhancing the intensity of room-temperature afterglow. These findings demonstrate that the $CsCdCl_3$:Mn^{2+}/Sb^{3+} crystals are efficient materials for storing electrons, and the additional introduction of Sb ions can adjust the defect depth to achieve persistent radioluminescence at room temperature. Fig. 3c and Fig. S12 (ESI†) illustrate the evolution of luminescence intensity in $CsCdCl_3$:Mn^{2+}/Sb^{3+} with changes in temperature under UV and X-ray excitation. Before 500 K, the radioluminescence

intensity of $CsCdCl_3:Mn^{2+}/Sb^{3+}$ exhibited a trend of initially increasing and then decreasing intensity. Even at 493 K, the luminous intensity of the sample still reached 96.63%. In contrast, $CsCdCl_3:Mn^{2+}$ intensity exhibited a linear decrease in radioluminescence intensity. The exceptional resistance to thermal quenching observed in $CsCdCl_3:Mn^{2+}/Sb^{3+}$ can be attributed to the rigid lattice structure, which reduces the probability of electron–phonon coupling (Table S4, ESI†).[52,53] Additionally, electrons in the defects are transferred to Sb and Mn *via* thermal excitation, compensating for the temperature-induced non-radiative transitions. To gain further insights into the regulatory effects of Sb and Mn doping on radiation luminescence and defects, we employed density functional theory (DFT) to calculate the electronic structure and band structure. The top of valence band in $CsCdCl_3:Mn^{2+}/Sb^{3+}$ is notably flatter compared to $CsCdCl_3:Mn^{2+}$, indicating that the co-doping strategy of Sb and Mn enhances localized electronic energy dispersion, resulting in an indirect band gap of 1.34 eV, similar to $CsCdCl_3:Mn^{2+}$ of 1.35 eV (Fig. 3d and Fig. S13a, b, ESI†). In the $CsCdCl_3:Mn^{2+}$ crystal lattice, two types of hole traps shallow and deep are observed. The subsequent incorporation of Sb^{3+} not only increases the density of the pre-existing shallow trap states near the valence band but also introduces new shallow defects (Fig. 3e-f). Upon the introduction of Sb^{3+} ions into $CsCdCl_3:Mn^{2+}$, X-ray photoelectron spectroscopy (XPS) analysis reveals a shift in the F 1s core level toward lower binding energy (Fig. S13c, ESI†). This indicates a modification in the electron cloud distribution around the Cl ions attributed to the influence of Sb^{3+} ions. Moreover, the introduction of Sb^{3+} ions in $CsCdCl_3:Mn^{2+}$ crystal lattice may affect the distribution of hole defects.[51] Under X-ray excitation, the afterglow intensity increases with the X-ray dose (Fig. 3g). In contrast, the afterglow intensity of $CsCdCl_3:Mn^{2+}/Sb^{3+}$ crystals remain consistent, attributed to X-ray production of more charge carriers than UV.

Based on the experimental results, we propose a mechanism to regulate defect traps in the crystal field for achieving persistent radioluminescence at room temperature in $CsCdCl_3:Mn^{2+}/Sb^{3+}$ crystal. In this crystal, high-energy X-ray photons generate a large number of high-energy electrons through the photoelectric effect and Compton scattering. These high-energy electrons undergo conversion into low-momentum electrons through electron–electron scattering and Auger processes. Subsequently, a number of electrons accumulate in the conduction band and quickly transfer to Sb and Mn ions, resulting in composite luminescence with holes. Simultaneously, another fraction of the electrons is stored in shallow defects. The electrons stored in shallow defects can spontaneously and gradually transfer to the luminescence levels of Sb and Mn ions, while the

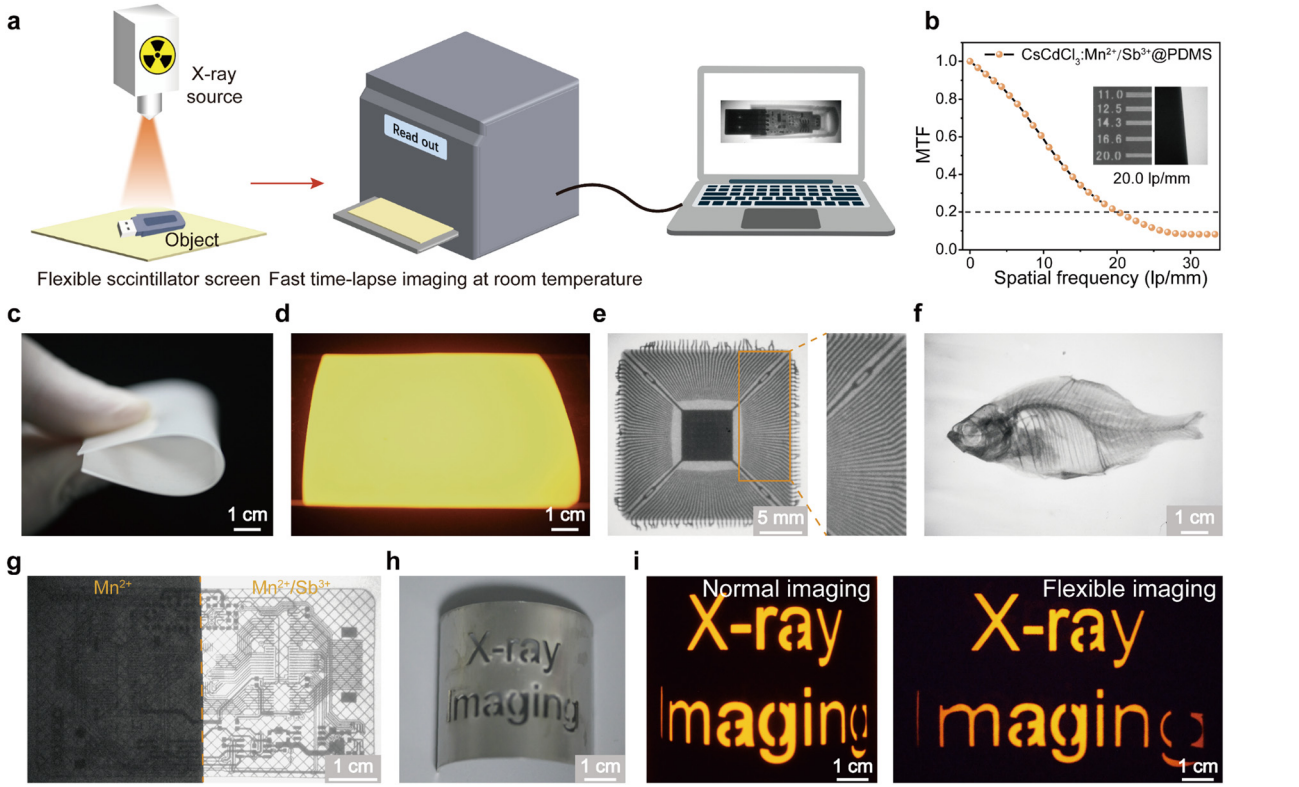

Fig. 4 Time-lapse X-ray imaging based on $CsCdCl_3:5\%Mn^{2+}/0.1\%Sb^{3+}$ crystal. (a) Schematic diagram of time-lapse X-ray imaging system. (b) MTF curves of the X-ray imaging. The inset showed the standard X-ray resolution pattern plate (from 11.0 to 20 lp mm^{-1}) partial imaging and the slanted-edge method used for MTF calculation. (c) Photograph of flexible scintillation screen bending in daylight. (d) Photograph of flexible scintillation screen under X-ray excitation. (e) X-ray image of the electronic chip. (f) The X-ray image of biological specimen. (g) Comparison of X-ray images of the flexible chip of the scintillation screen prepared by $CsCdCl_3:5\%Mn^{2+}$ (left) and $CsCdCl_3:5\%Mn^{2+}/0.1\%Sb^{3+}$ (right). (h) Bright-field photograph of the curved object. (i) Normal (left) and flexible X-ray images (right) of the curved object using the flexible scintillator screen.

electrons in deep defects are released through heat and light stimulation (Fig. 3h).

3.4. High-resolution time-lapse X-ray imaging

The capability of the $CsCdCl_3$:Mn^{2+}/Sb^{3+} crystal to emit persistent luminescence at room temperature holds promise for the development of a time-lapse X-ray imaging detector. We first prepared a flexible scintillation screen by uniformly mixing 60 wt% of ground $CsCdCl_3$:5%Mn^{2+}/0.1%Sb^{3+} powder into polydimethylsiloxane (PDMS) (Fig. S14a, ESI†). In the experimental setup, a target object was placed between the X-ray source and the flexible scintillation screen, and time-lapse X-ray imaging was recorded using a CMOS camera (Fig. 4a). The time-lapse X-ray imaging achieved by $CsCdCl_3$:Mn^{2+}/Sb^{3+} scintillation screen demonstrated high resolution of 20.0 lp mm^{-1}, as verified by a modulation transfer function (MTF) (Fig. 4b and Fig. S14b, c, ESI†). This high resolution surpasses that of most reported organic and inorganic scintillator materials.[54–59] Furthermore, the imaging capability of the scintillator screen as an X-ray detector was validated. The flexibility and brightness properties of $CsCdCl_3$:Mn^{2+}/Sb^{3+}@PDMS screen enable X-ray imaging of precision parts and non-planar objects (Fig. 4c and d). As shown in Fig. 4e, the internal structure of fine electronic chips is discernible. The bone spurs of the fish specimen are clearly distinguished. High-quality X-ray imaging of biological further confirms the potential application in medical diagnosis (Fig. 4f). Additionally, the flexible scintillation screen prepared using $CsCdCl_3$:Mn^{2+}/Sb^{3+} exhibits enhanced contrast and resolution for electronic chips (Fig. 4g). The flexible X-ray imaging approach circumvents the image distortions arising from the incongruity between a flat X-ray imaging surface and a curved object (Fig. 4h, i and Fig. S14d, ESI†). Finally, the bending resistance and ductility of scintillation screen were verified by tensile test, and the Young's modulus and extension limit were calculated at 9.7 Mpa and 122.5%, respectively (Fig. S15, ESI†).[60]

Conclusion

We have successfully developed an effective strategy for regulating the trap defects in crystal defects through heterovalent metal doping. By adjusting the defect location of $CsCdCl_3$:Mn^{2+} to room temperature, we achieved a significant increase in the intensity of persistent luminescence. The $CsCdCl_3$:5%Mn^{2+}/0.1%Sb^{3+} perovskite demonstrated excellent solvent, thermal, and radiation stability. Even at a temperature of 493 K, the integrated luminescence intensity of the sample remained at an impressive 96.63%, indicating remarkable resistance to thermal quenching. Furthermore, using its outstanding X-ray absorption capacity and persistent luminescence characteristics, $CsCdCl_3$:5%Mn^{2+}/0.1%Sb^{3+} crystals were uniformly mixed with PDMS to prepare a flexible scintillator screen to achieve time-lapse X-ray imaging with a high spatial resolution of reaching 20.0 lp mm^{-1}. These findings not only highlight the potential of $CsCdCl_3$:Mn^{2+}/Sb^{3+} crystal scintillators for time-lapsed X-ray imaging but also contribute valuable insights into the design principles for developing persistent luminescence scintillators.

Author contributions

Xiaokun Li: data curation, investigation, writing – original draft. Huixi Guo: data curation, investigation, formalanalysis. Yahuang Li: formal analysis, investigation. Caihou Lin: supervision, writing – review & editing. Lili Xie: supervision, funding acquisition, writing – review & editing.

Conflicts of interest

There are no conflicts to declare.

Acknowledgements

This work was supported by the National Natural Science Foundation of China (grant number 22204020), the Natural Science Foundation of Fujian Province (grant numbers 2021J01760, 2022J01709 and 2023J011173), Fujian Medical University's Research Foundation for Talented Scholars (Grant No. XRCZX2021022) and the Excellent Young Scholars Cultivation Project of Fujian Medical University Union Hospital (grant number 2022XH039).

References

1 Q. Chen, J. Wu, X. Ou, B. Huang, J. Almutlaq, A. A. Zhumekenov, X. Guan, S. Han, L. Liang, Z. Yi, J. Li, X. Xie, Y. Wang, Y. Li, D. Fan, D. B. L. Teh, A. H. All, O. F. Mohammed, O. M. Bakr, T. Wu, M. Bettinelli, H. Yang, W. Huang and X. Liu, All-inorganic perovskite nanocrystal scintillators, *Nature*, 2018, **561**, 88–93.

2 W. Chen, T. Chen and J. Fu, Pivotal role of organic materials in aqueous zinc-based batteries: regulating cathode, anode, electrolyte, and separator, *Adv. Funct. Mater.*, 2023, 2308015.

3 N. Zhang, L. Qu, S. Dai, G. Xie, C. Han, J. Zhang, R. Huo, H. Hu, Q. Chen, W. Huang and H. Xu, Intramolecular charge transfer enables highly-efficient X-ray luminescence in cluster scintillators, *Nat. Commun.*, 2023, **14**, 2901.

4 Y. Zhang, M. Chen, X. Wang, M. Lin, H. Wang, W. Li, F. Chen, Q. Liao, H. Chen, Q. Chen, M. Lin and H. Yang, Efficient and fast X-ray luminescence in organic phosphors through high-level triplet-singlet reverse intersystem crossing, *CCS Chem.*, 2023, **6**, 334–341.

5 H. Wang, C. Peng, M. Chen, Y. Xiao, T. Zhang, X. Liu, Q. Chen, T. Yu and W. Huang, Wide-range color-tunable organic scintillators for X-ray imaging through host-guest doping, *Angew. Chem., Int. Ed.*, 2023, **63**, e202316190.

6 Z. Yang, Q. Xu, Q. Chen and H. Yang, Breaking the boundaries of biological penetration depth: X-ray luminescence in light theranostics, *Sci. China Chem.*, 2024, 1–4.

7 Q. Wu, Q. Zheng, Y. He, Q. Chen and H. Yang, Emerging nanoagents for medical X-ray imaging, *Anal. Chem.*, 2023, **95**, 33–48.
8 X. Ou, X. Qin, B. Huang, J. Zan, Q. Wu, Z. Hong, L. Xie, H. Bian, Z. Yi, X. Chen, Y. Wu, X. Song, J. Li, Q. Chen, H. Yang and X. Liu, High-resolution X-ray luminescence extension imaging, *Nature*, 2021, **590**, 410–415.
9 L. Xie, Z. Hong, J. Zan, Q. Wu, Z. Yang, X. Chen, X. Ou, X. Song, Y. He, J. Li, Q. Chen and H. Yang, Broadband detection of X-ray, ultraviolet, and near-infrared photons using solution-processed perovskite-lanthanide nanotransducers, *Adv. Mater.*, 2021, **33**, 2101852.
10 H. Jiang, Q. Chen, H. Wang, T. Wu, J. Gong, Z. Zhang, Q. Chen, H. Yang and L. Xie, Efficient production of ligand-free microscintillators at gram-scale for high-resolution X-ray luminescence imaging, *Chin. Chem. Lett.*, 2023, **35**, 108899.
11 Z. Yang, P. Zhang, X. Chen, Z. Hong, J. Gong, X. Ou, Q. Wu, W. Li, X. Wang and L. Xie, High-confidentiality X-ray imaging encryption using prolonged imperceptible radioluminescence memory scintillators, *Adv. Mater.*, 2023, **35**, 2309413.
12 Y. Li, M. Gecevicius and J. Qiu, Long persistent phosphors-from fundamentals to applications, *Chem. Soc. Rev.*, 2016, **45**, 2090–2136.
13 Z. Li, Y. Zhang, X. Wu, L. Huang, D. Li, W. Fan and G. Han, Direct aqueous-phase synthesis of sub-10 nm ''luminous pearls'' with enhanced in vivo renewable near-infrared persistent luminescence, *J. Am. Chem. Soc.*, 2015, **137**, 5304–5307.
14 T. Matsuzawa, Y. Aoki, N. Takeuchi and Y. Murayama, A new long phosphorescent phosphor with high brightness, $SrAl_2O_4$:Eu^{2+}, Dy^{3+}, *J. Electrochem. Soc.*, 1996, **143**, 2670.
15 K. Hoang, C. Latouche and S. Jobic, Defect energy levels and persistent luminescence in Cu-doped ZnS, *Comput. Mater. Sci.*, 2019, **163**, 63–67.
16 Y. Liu, S. Yan, T. Wang, Q. He, X. Zhu, C. Wang, D. Liu, T. Wang, X. Xu and X. Yu, Achieving color-tunable long persistent luminescence in Cs_2CdCl_4 ruddlesden-popper phase perovskites, *Angew. Chem., Int. Ed.*, 2023, **62**, e202308420.
17 S.-Y. Yao, H. Li, M. Zhou, T.-C. Wang, X. Yu, Y.-S. Xu, J.-H. Yi, J.-B. Qiu, J. Yu and X.-H. Xu, Visualization of X-rays with an ultralow detection limit via zero-dimensional perovskite scintillators, *ACS Appl. Mater. Interfaces*, 2022, **14**, 56957–56962.
18 C. W. Hsu, B. Zhen, W. Qiu, O. Shapira, B. G. DeLacy, J. D. Joannopoulos and M. Soljačić, Transparent displays enabled by resonant nanoparticle scattering, *Nat. Commun.*, 2014, **5**, 3152.
19 S. Makarov, A. Furasova, E. Tiguntseva, A. Hemmetter, A. Berestennikov, A. Pushkarev, A. Zakhidov and Y. Kivshar, Halide-perovskite resonant nanophotonics, *Adv. Opt. Mater.*, 2019, **7**, 1800784.
20 Q. Zheng and L. Xie, Multifaceted luminescence in lanthanide-activated microrods for advanced multicolor anti-counterfeiting, *Mater. Chem. Front.*, 2024, **8**, 567–574.
21 S. Peng, P. Xia, T. Wang, L. Lu, P. Zhang, M. Zhou, F. Zhao, S. Hu, J. T. Kim and J. Qiu, Mechano-luminescence behavior of lanthanide-doped fluoride nanocrystals for three-dimensional stress imaging, *ACS Nano*, 2023, **17**, 9543–9551.
22 Z. Hong, Z. Chen, Q. Chen and H. Yang, Advancing X-ray luminescence for imaging, biosensing, and theragnostics, *Acc. Chem. Res.*, 2022, **56**, 37–51.
23 X. Wang, E. Song, L. Qin, D. Gui, Z. Xu, J. Xie, M. Lei, H. Zhang, Y. Wang and Y. Wang, Fabrication of a wide color gamut pc-WLED surpassing 107% NTSC based on a robust luminescent uranyl phosphate, *Chem. Mater.*, 2021, **33**, 6329–6337.
24 Y. Li, Y.-Y. Li, K. Sharafudeen, G.-P. Dong, S.-F. Zhou, Z.-J. Ma, M.-Y. Peng and J.-R. Qiu, A strategy for developing near infrared long-persistent phosphors: taking $MAlO_3$:Mn^{4+}, Ge^{4+} (M = La, Gd) as an example, *J. Mater. Chem. C*, 2014, **2**, 2019–2027.
25 Z. Pan, V. Castaing, L. Yan, L. Zhang, C. Zhang, K. Shao, Y. Zheng, C. Duan, J. Liu, C. Richard and B. Viana, Facilitating low-energy activation in the near-infrared persistent luminescent phosphor $Zn_{1+x}Ga_{2-2x}Sn_xO_4$:Cr^{3+} *via* crystal field strength modulations, *J. Phys. Chem. C*, 2020, **124**, 8347–8358.
26 T. Aitasalo, P. Dereń, J. Hölsä, H. Jungner, J. C. Krupa, M. Lastusaari, J. Legendziewicz, J. Niittykoski and W. Stręk, Persistent luminescence phenomena in materials doped with rare earth ions, *J. Solid State Chem.*, 2003, **171**, 114–122.
27 P. Dorenbos, Study of TL glow curves of YPO_4 double doped with lanthanide ions, *Radiat. Meas.*, 2011, **46**, 1410–1416.
28 A. J. J. Bos, P. Dorenbos, A. Bessière, A. Lecointre, M. Bedu, M. Bettinelli and F. Piccinelli, Solution-grown chloride perovskite crystal of red afterglow, *Angew. Chem., Int. Ed.*, 2021, **60**, 24450–24455.
29 W. Zheng, X. Li, N. Liu, S. Yan, X. Wang, X. Zhang, Y. Liu, Y. Liang, Y. Zhang and H. Liu, Solution-Grown Chloride Perovskite Crystal of Red Afterglow, *Angew. Chem., Int. Ed.*, 2021, **60**, 24450–24455.
30 A. K. Jena, A. Kulkarni and T. Miyasaka, Halide perovskite photovoltaics: background, status, and future prospects, *Chem. Rev.*, 2019, **119**, 3036–3103.
31 M. I. Saidaminov, O. F. Mohammed and O. M. Bakr, Low-dimensional-networked metal halide perovskites: the next big thing, *ACS Energy Lett.*, 2017, **2**, 889–896.
32 L. N. Quan, B. P. Rand, R. H. Friend, S. G. Mhaisalkar, T.-W. Lee and E. H. Sargent, Perovskites for next-generation optical sources, *Chem. Rev.*, 2019, **119**, 7444–7477.
33 F. Zhang, Y. Zhou, Z. Chen, M. Wang, Z. Ma, X. Chen, M. Jia, D. Wu, J. Xiao, X. Li, Y. Zhang, Z. Shi and C. Shan, Thermally activated delayed fluorescence zirconium-based perovskites for large-area and ultraflexible X-ray scintillator screens, *Adv. Mater.*, 2022, **34**, 2204801.
34 K. Han, J. Qiao, S. Zhang, B. Su, B. Lou, C.-G. Ma and Z. Xia, Band alignment engineering in ns^2 electrons doped metal halide perovskites, *Laser Photonics Rev.*, 2023, **17**, 2200458.
35 Z. Liu, L. Zhao, X. Yang, L. Yang, H. Zhang, W. Zeng, X. Yu, J. Qiu and X. Xu, Long persistent luminescence properties of

NaBaScSi2O7:Tb^{3+} and it's applications above room temperature, *Chem. Eng. J.*, 2020, **401**, 126119.

36 X. Yu, S. Wang, Y. Zhu, J. Liang, J. Qiu, X. Xu and W. Lu, High-temperature long persistent and photo-stimulated luminescence in Tb^{3+} doped gallate phosphor, *J. Alloys Compd.*, 2017, **701**, 774–779.

37 Y. Zhuang, J. Ueda and S. Tanabe, Tunable trap depth in $Zn(Ga_{1-x}Al_x)_2O_4$:Cr,Bi red persistent phosphors: considerations of high-temperature persistent luminescence and photostimulated persistent luminescence, *J. Mater. Chem. C*, 2013, **1**, 7849–7855.

38 X. Zhou, K. Han, Y. Wang, J. Jin, S. Jiang, Q. Zhang and Z. Xia, Energy-trapping management in X-ray storage phosphors for flexible 3D imaging, *Adv. Mater.*, 2023, **35**, 2212022.

39 S. Ge, H. Peng, Q. Wei, X. Shen, W. Huang, W. Liang, J. Zhao and B. Zou, Realizing color-tunable and time-dependent ultralong afterglow emission in antimony-doped $CsCdCl_3$ metal halide for advanced anti-counterfeiting and information encryption, *Adv. Opt. Mater.*, 2023, **11**, 2300323.

40 W. Jia, Q. Wei, S. Ge, C. Peng, T. Huang, S. Yao, Y. Tian, T. Chang, R. Zeng and B. Zou, Polaronic magnetic excitons and photoluminescence in Mn^{2+}-Doped $CsCdBr_3$ metal halides, *J. Phys. Chem. C*, 2021, **125**, 18031–18039.

41 Q. Guo, X. Zhao, B. Song, J. Luo and J. Tang, Light emission of self-trapped excitons in inorganic metal halides for optoelectronic applications, *Adv. Mater.*, 2022, **34**, 2201008.

42 H.-P. Wang, S. Li, X. Liu, Z. Shi, X. Fang and J.-H. He, Low-dimensional metal halide perovskite photodetectors, *Adv. Mater.*, 2021, **33**, 2003309.

43 Z. Ma, X. Ji, M. Wang, F. Zhang, Z. Liu, D. Yang, M. Jia, X. Chen, D. Wu, Y. Zhang, X. Li, Z. Shi and C. Shan, Carbazole-containing polymer-assisted trap passivation and hole-injection promotion for efficient and stable $CsCu_2I_3$-based yellow LEDs, *Adv. Sci.*, 2022, **9**, 2202408.

44 C. Zhou, Y. Tian, M. Wang, A. Rose, T. Besara, N. K. Doyle, Z. Yuan, J. C. Wang, R. Clark, Y. Hu, T. Siegrist, S. Lin and B. Ma, Low-dimensional organic tin bromide perovskites and their photoinduced structural transformation, *Angew. Chem., Int. Ed.*, 2017, **56**, 9018–9022.

45 A. Kudlu, D. Kumar Das, R. Bakthavatsalam, J. Sam, S. Ray, P. Mondal, S. Dutta, V. R. Hathwar, R. Pallepogu and J. Kundu, Strong dopant-dopant electronic coupling in emissive codoped two dimensional metal halide hybrid, *J. Phys. Chem. Lett.*, 2023, **14**, 4933–4940.

46 G. Dai, Z. Ma, Y. Qiu and Z. Ma, Codoped 2D all-inorganic halide perovskite $Cs_3Cd_2C_{l7}$:Sb^{3+}:Mn^{2+} with ultralong afterglow, *Inorg. Chem.*, 2023, **62**, 7906–7913.

47 O. D. Moseley, T. A. Doherty, R. Parmee, M. Anaya and S. D. Stranks, Halide perovskites scintillators: unique promise and current limitations, *J. Mater. Chem. C*, 2021, **9**, 11588–11604.

48 X. Wang, H. Shi, H. Ma, W. Ye, L. Song, J. Zan, X. Yao, X. Ou, G. Yang, Z. Zhao, M. Singh, C. Lin, H. Wang, W. Jia, Q. Wang, J. Zhi, C. Dong, X. Jiang, Y. Tang, X. Xie, Y. Yang, J. Wang, Q. Chen, Y. Wang, H. Yang, G. Zhang, Z. An, X. Liu and W. Huang, Organic phosphors with bright triplet excitons for efficient X-ray-excited luminescence, *Nat. Photon.*, 2021, **15**, 187–192.

49 Y. Zhuang, D. Chen, W. Chen, W. Zhang, X. Su, R. Deng, Z. An, H. Chen and R.-J. Xie, X-ray-charged bright persistent luminescence in $NaYF_4$:Ln^{3+}@NaYF4 nanoparticles for multidimensional optical information storage, *Light Sci. Appl.*, 2021, **10**, 132.

50 J. Xiahou, Q. Zhu, L. Zhu, S. Li and J.-G. Li, Local structure regulation in near-infrared persistent phosphor of $ZnGa_2O_4$:Cr^{3+} to fabricate natural-light rechargeable optical thermometer, *ACS Appl. Electron. Mater.*, 2021, **3**, 3789–3803.

51 L. Wang, D. Tu, C. Li, S. Han, F. Wen, S. Yu, X. Yi, Z. Xie and X. Chen, Engineering trap distribution to achieve multicolor persistent and photostimulated luminescence from ultraviolet to near-infrared II, *Matter*, 2023, **6**, 4261–4273.

52 H. Maimaitizi, D. Li, A. Abulizi, S. Halifu, T. Ye and G. Chen, Heterostructure $CsPbBr_3$/SrBrF nanocrystals stabilize perovskite LEDs with suppressed halogen ion migration, *ACS Mater. Lett.*, 2023, **6**, 250–259.

53 B. Ghebouli, M. Ghebouli, M. Fatmi and A. Bouhemadou, First-principles study of the structural, elastic, electronic, optical and thermodynamic properties of the cubic perovskite $CsCdCl_3$ under high pressure, *Solid State Commun.*, 2010, **150**, 1896–1901.

54 H. Wei and J. Huang, Halide lead perovskites for ionizing radiation detection, *Nat. Commun.*, 2019, **10**, 1066.

55 P. Büchele, M. Richter, S. F. Tedde, G. J. Matt, G. N. Ankah, R. Fischer, M. Biele, W. Metzger, S. Lilliu, O. Bikondoa, J. E. Macdonald, C. J. Brabec, T. Kraus, U. Lemmer and O. Schmidt, X-ray imaging with scintillator-sensitized hybrid organic photodetectors, *Nat. Photon.*, 2015, **9**, 843–848.

56 H. Zhang, Z. Yang, M. Zhou, L. Zhao, T. Jiang, H. Yang, X. Yu, J. Qiu, Y. Yang and X. Xu, Reproducible X-ray imaging with a perovskite nanocrystal scintillator embedded in a transparent amorphous network structure, *Adv. Mater.*, 2021, **33**, 2102529.

57 T. He, Y. Zhou, X. Wang, J. Yin, L. Gutiérrez-Arzaluz, J.-X. Wang, Y. Zhang, O. M. Bakr and O. F. Mohammed, High-performance copper-doped perovskite-related silver halide X-ray imaging scintillator, *ACS Energy Lett.*, 2022, **7**, 2753–2760.

58 W. Ma, Y. Su, Q. Zhang, C. Deng, L. Pasquali, W. Zhu, Y. Tian, P. Ran, Z. Chen, G. Yang, G. Liang, T. Liu, H. Zhu, P. Huang, H. Zhong, K. Wang, S. Peng, J. Xia, H. Liu, X. Liu and Y. M. Yang, Thermally activated delayed fluorescence (TADF) organic molecules for efficient X-ray scintillation and imaging, *Nat. Mater.*, 2022, **21**, 210–216.

59 J.-X. Wang, L. Gutiérrez-Arzaluz, X. Wang, T. He, Y. Zhang, M. Eddaoudi, O. M. Bakr and O. F. Mohammed, Heavy-atom engineering of thermally activated delayed fluorophores for high-performance X-ray imaging scintillators, *Nat. Photon.*, 2022, **16**, 869–875.

60 S. Zhu, S. Wang, Y. Huang, Q. Tang, T. Fu, R. Su, C. Fan, S. Xia, P. S. Lee and Y. Lin, Bioinspired structural hydrogels with highly ordered hierarchical orientations by flow-induced alignment of nanofibrils, *Nat. Commun.*, 2024, **15**, 118.

